

# Review Report - Fourth Quarter 2023: Analysis and Design of Spatial Mechanisms of Tensegrity for Collaborative Manipulation

Karol Muñoz, Mathieu Porez, Philippe Wenger

## ▶ To cite this version:

Karol Muñoz, Mathieu Porez, Philippe Wenger. Review Report - Fourth Quarter 2023: Analysis and Design of Spatial Mechanisms of Tensegrity for Collaborative Manipulation. Centrale Nantes; IMT Atlantique. 2024. hal-04405080v2

# HAL Id: hal-04405080 https://hal.science/hal-04405080v2

Submitted on 24 Jan 2024

HAL is a multi-disciplinary open access archive for the deposit and dissemination of scientific research documents, whether they are published or not. The documents may come from teaching and research institutions in France or abroad, or from public or private research centers. L'archive ouverte pluridisciplinaire **HAL**, est destinée au dépôt et à la diffusion de documents scientifiques de niveau recherche, publiés ou non, émanant des établissements d'enseignement et de recherche français ou étrangers, des laboratoires publics ou privés.

Copyright

PhD Student: Karol Muñoz Salas

Supervisors: Philippe Wenger and Mathieu Porez

**Abstract** This report presents the kinematic, static and stability analysis of a new perspective of a three-degrees-of-freedom (3-DOF) spatial mechanism. The mechanism uses a simple architecture of bars, cables, platforms and spherical joints, making it lightweight and suitable for integration into a stack of a robot manipulator. Analysis in three dimensional space with fixed internal DOF reveals instability. It is concluded that the addition of a new cable between the centres of the platforms and the correct adjustment of its tension is necessary to ensure stability, especially during rotation against gravity, and also limit the number of DOF to 2.

#### 1 Introduction

Over the past decade, our businesses have undergone a profound transformation in production methodologies, incorporating digital tools such as the cloud, AI, and AR to boost productivity and sustain competitiveness [1].

Robotics, especially collaborative industrial robots (cobots), has emerged as a key driver in this new industrial era [2]. These cobots, working collaboratively with operators at workstations, excel in tasks like assembling complex systems, operating in extreme conditions, and handling heavy objects that require processing or storage. Apart from enhancing production rates, they also serve as a protective shield for operators against musculoskeletal disorders (MSDs). However, the versatility of these "Swiss Army knives" comes with inherent risks. Substantial differences in mass and rigidity mean that a collision between a cobot and a human could have fatal consequences [3]. To ensure operator safety and optimize the benefit-risk ratio of utilizing robotics in industry, innovative adaptive kinematics for robots must be proposed. These kinematics should strike a balance between being sufficiently rigid for precise operation in a confined workspace and flexible enough to move safely within the area occupied by an operator [4].

The commitment to crash safety necessitates that only controlled or 'safe' collisions occur among robots, humans, and obstacles. The primary goal is to limit the power/force exerted on humans, requiring a more compliant control strategy. Given the constraint of a very limited working area for both humans and robots, the use of overhead cameras for supervision is deemed impractical and expensive. Consequently, power and force-limiting techniques must be implemented, along with reduced speed and secure monitoring of the robot's speed and position.

Addressing this challenge, our focus lies on tensegrity mechanisms, a topic gaining prominence in robotics. Inspired by the musculoskeletal system of animals, tensegrity structures originated as a design trend in the 1960s [5, 6, 7]. These lightweight mechanical structures result from balancing bars in compression and cables in tension. The geometric configuration, rigidity, and stability of the system can be finely tuned for its intended use by adjusting the tension intensity within the structure through co-actuation of cables. Therefore, the field of tensegrity holds promise in finding design solutions for creating robots that are both rigid for precise operation and flexible to work seamlessly with operators.

## 2 Proposed Spatial Mechanism

This section aims to provide background information that led to the proposed spatial mechanism design and introduce its characteristics and parameters. Subsection 2.1 will present the research background, considering the concept of tensegrity and its applications, with a particular focus on robotics. In addition, a general presentation of the proposed spatial mechanism resulting from this research will be given. Subsection 2.2 will present the detailed characteristics of the proposed mechanism, providing insights into its application for the analyses performed in the following chapters.

#### 2.1 Background

Tensegrity systems have found widespread application in fields as diverse as aerospace, architecture, civil engineering and biological systems modelling. Their unique properties, including lightness, adaptability, flexibility, mass efficiency and the ability to control structural configurations, make them versatile for diverse applications in nature, art, architecture, engineering and science [8].

In the field of robotics, tensegrity has become a preferred choice for robot design, capitalising on its ability to provide high precision while maintaining flexibility for example through bio-inspired designs. Liu et al. [9] assessed the current landscape of tensegrity-based robots, covering design, fabrication, modelling, analysis and motion control. While challenges remain, notable progress has been made, motivating our search for optimal robot design in a human-machine workspace.

Burkhardt's work [10] introduced the t-prism, a simple yet fundamental tensegrity structure. This research investigates this structure, exploring its construction using dowels, fishing lines and cylindrical coordinates. The optimisation problem focuses on minimising the length of the side tendons while satisfying constraints on radius, strut length and symmetry. Arsenault and Gosselin [11] proposed a 3-DOF positional tensegrity mechanism with a modular design, reduced inertia, and a large workspace. It is treated as an assembly of independent elements based on Snelson's X-shaped tensegrity system [6]. The limits of the actuator workspace reveal limitations for mechanisms with three or more modules. Marshall [12] introduced a parallel platform device based on tensegrity principles. It replaces elements with variable length legs and combinations of springs and connectors. The analysis confirms the configurability of the upper platform by externally applied wrench coordinates. Furet [13] and Fasquelle [14] used antiparallelogram tensegrity joints to model a bird neck. Mirats and Camps [15] presented a tensegrity-based robot with a 3-bar symmetric prismatic configuration anchored to the ground. Despite being underactuated, the robot exhibits controlled motion within its workspace. The study highlights the singularity of equilibrium matrices for stable configurations and anticipates future work on control laws and hyper-actuated structures, demonstrating the potential of tensegrity in deformable and adaptive robots. Fasquelle et al. [16] presented lightweight manipulators using anti-parallelogram X-joints to form a tensegrity mechanism with one degree of freedom. This design, inspired by the musculoskeletal structure of the bird's neck, is validated through simulation and experimentation on a test-bed prototype, offering intrinsic stability, variable stiffness and lower inertia compared to conventional manipulators. Kim [17] proposed a compact 2-DOF cable-driven wrist joint. John [18] noticed that this wrist joint has theoretical mobility of 0 and that the practical mobility is only provided by link deformations and clearances. He then proposed a new variant to overcome this issue. Their work presents a new variant of the quaternion joint and contributes to the advancement of tensegrity-based robotic manipulators in bio-inspired robotics.

Inspired by this body of research, our proposed 3-DOF spatial mechanism, shown in Fig 1, promises interesting insights. The ultimate goal of this research is to integrate a stack of these mechanisms, as shown in Fig 2, to construct a robotic manipulator.





**Fig. 1** CAD and prototype for the proposed mechanism.



**Fig. 2** Robot manipulator using a stack of the proposed spatial mechanism.

## 2.2 Description

Fig. 3 shows the CAD model of the 3-DOF spatial manipulator. The configuration consists of two different platforms. **Bottom or fixed platform:** This platform remains fixed and is characterised by six vertices:  $A_1$ ,  $B_1$ ,  $A_2$ ,  $B_2$ ,  $A_3$ ,  $B_3$ . Its equidistant centre is denoted by  $o_0$ . The points  $A_i$  are placed at a uniform distance b from each other, forming an angle  $\psi$  between  $A_i$  and  $B_i$ . **Upper or mobile platform:** The upper platform is mobile and also has six vertices:  $A_4$ ,  $B_5$ ,  $A_5$ ,  $B_6$ ,  $A_6$ ,  $B_4$ . The equidistant centre for this platform is denoted  $o_3$ . Similar to the lower platform, the distance between the points  $A_i$  is b, but with an angle of  $-\psi$  between  $A_i$  and  $B_i$ .

These two platforms are connected by three bars of equal length L. Specifically, the connections are as follows  $A_1$  to  $A_6$ ,  $A_2$  to  $A_4$  and  $A_3$  to  $A_3$ . In addition, the structure includes three cables of lengths  $l_1$ ,  $l_2$  and  $l_3$  connecting the vertices  $B_1$  to  $B_4$ ,  $B_2$  to  $B_5$  and  $B_3$  to  $B_6$  respectively.

Three reference frames are defined:  $\mathcal{F}_g = (o_g, \mathbf{s_g}, \mathbf{n_g}, \mathbf{a_g})$ ,  $\mathcal{F}_0 = (o_0, \mathbf{s_0}, \mathbf{n_0}, \mathbf{a_0})$ , and  $\mathcal{F}_3 = (o_3, \mathbf{s_3}, \mathbf{n_3}, \mathbf{a_3})$ , as visualised in Fig. 3. Here  $\mathcal{F}_g$  represents the general reference plane,  $\mathcal{F}_0$  is fixed to the lower platform and  $\mathcal{F}_3$  is on the upper platform.

Since the proposed mechanism is designed to be used as a joint in a series arrangment of such mechanisms (see Fig 1, right), two angular parameters  $\alpha$  and  $\beta$  are used to define its orientation in space.

Examining the proposed spatial mechanism in this context provides valuable insights into its kinematic and static analyses, as well as its stability. In the following sections, these aspects will be fully explored.

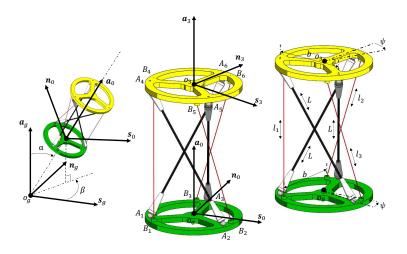


Fig. 3: Proposed Spatial Mechanism

## 3 Kinematic Model

This section explores the kinematic model that governs the proposed spatial mechanism, using the representation of its orientation workspace in terms of tilt and torsion angles. Subsection 3.1 introduces the use of tilt and torsion, providing their definitions in the context of the proposed mechanism. Subsection 3.2 introduces the inverse kinematic model. The inherent nonlinearity of parallel and spatial mechanisms, compounded by intricate interactions between actuators and variations in cables, poses a formidable challenge to the mathematical expression of their direct kinematic behaviour [19]. Consequently, we formulate the inverse kinematic model by integrating trilateration techniques and cable length determination. Furthermore, subsection 3.3 presents an exploration of the kinematic workspace, including an analysis of bar intersections and the identification of achievable values for spatial angles. Finally, subsection 3.4 delves into stability considerations, explaining the critical criteria for selecting cable lengths to ensure stability and the strategic placement of cables on the platforms.

#### 3.1 Tilt and Torsion

The orientation workspace of this spatial mechanism encompasses the array of viable 3-D orientations for the mobile platform at  $o_3$  in Cartesian coordinates. Similar to other parallel mechanisms, this spatial mechanism faces the challenge of accurately representing its orientation workspace due to the intricacies of interconnected and non-Euclidean rotational motion, as well as the inherent singularity present in any 3-D orientation parameterisation, such as the well-known set of Euler angles.

Nevertheless, Bonev's investigation [7] convincingly highlights the advantages of using tilt and torsion angles, as shown in Fig. 4, and confirms their suitability for a wide range of spatial and parallel mechanism applications. The inclusion of these innovative parameters results in a concise and highly intuitive representation of the orientation workspace, especially when modelling the motion limits of the mechanism studied in this research.

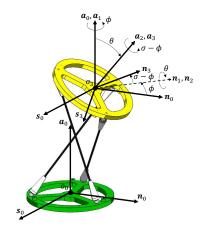


Fig. 4: Tilt and torsion parametrization.

Following [7], the rotation matrix  ${}^{0}R_{3}$  between  $\mathcal{F}_{0}$  and  $\mathcal{F}_{3}$  is given by:

$${}^{0}R_{3} = \operatorname{rot}(a_{0}, \phi)\operatorname{rot}(n_{1}, \theta)\operatorname{rot}(s_{2}, \sigma - \phi), \tag{1}$$

where:

$$\operatorname{rot}(a_{0}, \phi) = \begin{pmatrix} \cos \phi - \sin \phi & 0 \\ \sin \phi & \cos \phi & 0 \\ 0 & 0 & 1 \end{pmatrix},$$

$$\operatorname{rot}(n_{1}, \theta) = \begin{pmatrix} \cos \theta & 0 \sin \theta \\ 0 & 1 & 0 \\ -\sin \theta & 0 \cos \theta \end{pmatrix} \quad \text{and}$$

$$\operatorname{rot}(s_{2}, \sigma - \phi) = \begin{pmatrix} \cos(\sigma - \phi) - \sin(\sigma - \phi) & 0 \\ \sin(\sigma - \phi) & \cos(\sigma - \phi) & 0 \\ 0 & 0 & 1 \end{pmatrix},$$

$$(2)$$

and these three unit rotations around  $a_0$ ,  $n_1$ , and  $s_2$  define the tilt for the first two and the torsion for the last one.

#### 3.2 Inverse Kinematic Model

The inverse kinematic model is obtained in two steps (Fig. 5). The first step, called trilateration, involves computing the coordinates of the top platform  $(X,Y,Z)^T$  in the frame  $\mathcal{F}_3 = (o_3, \mathcal{B}_3)$ , where  $\mathcal{B}_3$  is the vector base  $(\mathbf{s_3}, \mathbf{n_3}, \mathbf{a_3})$  (Fig. 3). The second step is to determine the cable lengths  $l_i$  based on the spatial angles  $(\phi, \theta, \sigma)$ . This subsection provides a detailed exploration of both steps.

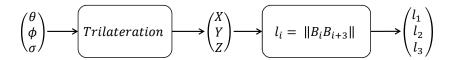


Fig. 5: Inverse kinematic model strategy.

We begin by deriving the position of the upper platform as a function of spatial angles. It takes into account the three geometric constraints imposed by the legs on the upper platform, namely  $L^2 = ||A_1A_6||^2$ ,  $L^2 = ||A_2A_4||^2$  and  $L^2 = ||A_3A_5||^2$ . In terms of  $(X, Y, Z)^T$ , these constraints can be expressed as:

$$\begin{pmatrix} 1 & 1 & 1 \\ 1 & 1 & 1 \\ 1 & 1 & 1 \end{pmatrix} \begin{pmatrix} X^2 \\ Y^2 \\ Z^2 \end{pmatrix} - 2 \begin{pmatrix} x_{\mathcal{S}_1} & y_{\mathcal{S}_1} & z_{\mathcal{S}_1} \\ x_{\mathcal{S}_2} & y_{\mathcal{S}_2} & z_{\mathcal{S}_2} \\ x_{\mathcal{S}_3} & y_{\mathcal{S}_3} & z_{\mathcal{S}_3} \end{pmatrix} \begin{pmatrix} X \\ Y \\ Z \end{pmatrix} + \begin{pmatrix} x_{\mathcal{S}_1}^2 + y_{\mathcal{S}_1}^2 + z_{\mathcal{S}_1}^2 - L^2 \\ x_{\mathcal{S}_2}^2 + y_{\mathcal{S}_2}^2 + z_{\mathcal{S}_2}^2 - L^2 \\ x_{\mathcal{S}_3}^2 + y_{\mathcal{S}_3}^2 + z_{\mathcal{S}_3}^2 - L^2 \end{pmatrix} = 0,$$
 (3)

where  $o_{s1} = (x_{S_1}, y_{S_1}, z_{S_1})^T$ ,  $o_{s2} = (x_{S_2}, y_{S_2}, z_{S_2})^T$  and  $o_{s3} = (x_{S_3}, y_{S_3}, z_{S_3})^T$  are the coordinates of the centres of the three spheres denoted  $S_1$ ,  $S_2$  and  $S_3$  (Fig. 6), each with a radius of L, intersecting at  $S_3$ . The trilateration method is then used to

solve equation (3), similar to the approach used by the authors in [20]. They used this mathematical method to model the kinematics of a delta robot.

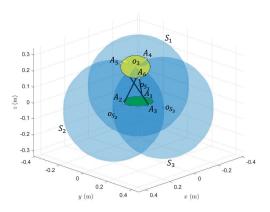


Fig. 6: Geometric constraints.

Considering, as in Fig.7, the three circles coming from the intersection of the spheres and the plane containing the upper platform, from (3), the equation of the circle  $C_i$  coming from  $S_i$  is the following:

$$\rho_i^2 = (X - x_{S_i})^2 + (Y - y_{S_i})^2, \tag{4}$$

where  $\rho_i^2 = L^2 - Z^2 + 2Zz_{0i} - z_{0i}^2$  is the radius of the circle  $S_i$ . Subtracting the equation of  $C_3$  from those of  $C_1$  and  $C_2$  gives the following linear system:

$$\begin{pmatrix} A_{11} & A_{12} \\ A_{21} & A_{22} \end{pmatrix} \begin{pmatrix} X \\ Y \end{pmatrix} = \begin{pmatrix} B_1 \\ B_2 \end{pmatrix} Z + \begin{pmatrix} C_1 \\ C_2 \end{pmatrix}, \tag{5}$$

where  $A_{11} = x_{S_1} - x_{S_2}$ ,  $A_{12} = y_{S_1} - y_{S_2}$ ,  $A_{21} = x_{S_1} - x_{S_3}$ ,  $A_{22} = y_{S_1} - y_{S_3}$ ,  $B_1 = 2(z_{S_2} - z_{S_1})$ ,  $B_2 = 2(z_{S_3} - z_{S_1})$ ,  $C_1 = x_{S_1}^2 - x_{S_2}^2 + y_{S_1}^2 - y_{S_2}^2 - z_{S_2}^2 + z_{S_1}^2$ , and  $C_2 = x_{S_1}^2 - x_{S_3}^2 + y_{S_1}^2 - y_{S_3}^2 - z_{S_3}^2 + z_{S_1}^2$ . As a function of Z the unique solvable pair (X, Y) of (5) is equal to:

$$X = \alpha_X Z + \beta_X, Y = \alpha_Y Z + \beta_Y, \tag{6}$$

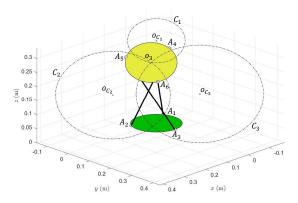


Fig. 7: Trilateration approach at  $\phi = \pi/6$ ,  $\theta = \pi/4$  and  $\sigma = -\pi/6$ .

where  $\alpha_X = (A_{22}B_1 - A_{12}B_2)/\det(A)$ ,  $\beta_X = (A_{12}C_2 - A_{22}C_1)/\det(A)$ ,  $\alpha_Y = (A_{11}B_2 - A_{21}B_1)/\det(A)$ , and  $\beta_Y = (A_{11}C_2 - A_{21}C_1)/\det(A)$ . Replacing, in the equation of  $C_3$ , X and Y by the solution pair (6), we obtain a second order equation as a function of Z, i.e:

$$0 = (1 + \alpha_X^2 + \alpha_Y^2)Z^2 + 2(\alpha_X(\beta_X - x_{S_1}) + \alpha_y(\beta_y - y_{S_1}) - z_{S_1})Z + ((\beta_X - x_{S_1})^2 + (\beta_Y - y_{S_1})^2 + z_{S_1}^2 - L^2),$$
(7)

which gives two or zero solutions as a function of  $(\phi, \theta, \sigma)$  and the mechanism parameters b and L. Once the values of Z are known, the solution pairs (X, Y) can be computed by (6). Fig. 8 shows an example of the result of this process. In this case both solutions of the inverse kinematic model are shown for  $\theta = \pi/4$  rad,  $\phi = \pi/6$  rad and  $\sigma = -\pi/6$  rad. It is important to note that there is no symmetry between the two solutions.

The second step to obtain the inverse kinematic model is to determine the length of the cables as a function of  $\theta$ ,  $\phi$  and  $\sigma$ . This is done using the cable length equation:  $l^2 = ||B_1B_4||^2$ ,  $l^2 = ||B_2B_5||^2$  and  $l^2 = ||B_3B_6||^2$ . Having obtained the values of  $\mathbf{B}_i$  (derived from the previous step) for both solutions, the lengths of the cables  $l_1$ ,  $l_2$  and  $l_3$  can be determined for each solution.

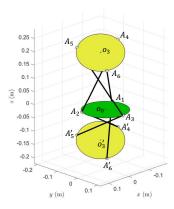


Fig. 8: Two solutions of the inverse kinematic model for  $\phi = \pi/6$  rad,  $\theta = \pi/4$  rad and  $\sigma = -\pi/6$  rad.

### 3.3 Kinematic Workspace

This subsection analyses the kinematic workspace of the mechanism by detecting the intersection of the bars using the inverse kinematic model. For this reason, a specific geometry is defined for the proposed mechanism, which will be used in the research from now on. Table 1 lists the parameters and their corresponding values for the proposed mechanism.

Table 1: Parameters, symbols and values for the proposed mechanism

Parameter	Symbol	Value
Distance between points $A_i$	b	15 cm
Angle between $A_i$ and $B_i$	$\psi$	$15^{\circ} (\pi/12 \text{ rad})$
Length of the bars	L	30 cm
Diameter of the bars	$D_b$	5 mm

In this context, determining the kinematic workspace involves calculating the distances between the bars and comparing them with a predefined threshold. The threshold is defined by the diameter of the bar  $D_b$  as specified in Table 1. These

distances, expressed as functions of  $\theta$ ,  $\phi$  and  $\sigma$ , make it possible to identify the values for which the distance exceeds the diameter. This indicates the absence of intersections, which represent the angles at which the mechanism can move.

The unit vectors  $\mathbf{v}$ ,  $\mathbf{u}$ ,  $\mathbf{w}$  correspond to bar 1  $(A_1A_6)$ , bar 2  $(A_2A_4)$  and bar 3  $(A_3A_5)$  respectively, as shown in Fig. 9. Using the inverse kinematic model, each of these vectors is expressed as a function of  $\theta$ ,  $\phi$  and  $\sigma$ .

$$\mathbf{u} = \frac{\mathbf{A}_6 - \mathbf{A}_1}{\|\mathbf{A}_6 - \mathbf{A}_1\|}, \mathbf{v} = \frac{\mathbf{A}_4 - \mathbf{A}_2}{\|\mathbf{A}_4 - \mathbf{A}_2\|} \text{ and } \mathbf{w} = \frac{\mathbf{A}_5 - \mathbf{A}_3}{\|\mathbf{A}_5 - \mathbf{A}_3\|}.$$
 (8)

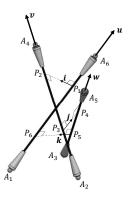


Fig. 9: The two solutions of the inverse kinematic model for  $\phi = \pi/6$ ,  $\theta = \pi/4$  and  $\sigma = -\pi/6$ .

Then the normal vectors are calculated for each pair of bars. The vector  $\mathbf{i}$  represents the normal vector between bar 1 and bar 2,  $\mathbf{j}$  represents the normal vector between bar 2 and bar 3, and finally  $\mathbf{k}$  represents the normal vector between bar 3 and bar 1, i.e:

$$\mathbf{i} = \mathbf{u} \times \mathbf{v}, \, \mathbf{j} = \mathbf{v} \times \mathbf{w} \text{ and } \mathbf{k} = \mathbf{w} \times \mathbf{u}.$$
 (9)

Consider  $P_1$  and  $P_6$  as arbitrary points on bar 1,  $P_2$  and  $P_3$  as arbitrary points on bar 2 and  $P_4$  and  $P_5$  as arbitrary points on bar 3 (Fig. 9). These points can be defined as follows.

$$\mathbf{P}_{1} = \mathbf{A}_{1} + \zeta_{1} \mathbf{u}, \mathbf{P}_{2} = \mathbf{A}_{2} + \zeta_{2} \mathbf{v}, \mathbf{P}_{3} = \mathbf{A}_{2} + \zeta_{3} \mathbf{v}, 
\mathbf{P}_{4} = \mathbf{A}_{3} + \zeta_{4} \mathbf{w}, \mathbf{P}_{5} = \mathbf{A}_{3} + \zeta_{5} \mathbf{w} \text{ and } \mathbf{P}_{6} = \mathbf{A}_{1} + \zeta_{6} \mathbf{u}.$$
(10)

In (10),  $\zeta_1$ ,  $\zeta_2$ ,  $\zeta_3$ ,  $\zeta_4$ ,  $\zeta_5$  and  $\zeta_6$  represent scalar parameters indicating the relative positions of points  $P_1$ ,  $P_2$ ,  $P_3$ ,  $P_4$ ,  $P_5$  and  $P_6$  along the directions of the vectors  $\mathbf{u}$ ,  $\mathbf{v}$  and  $\mathbf{w}$  respectively. Let  $d_1$  be defined as the minimum distance between the point  $P_1$  and the point  $P_2$ ,  $d_2$  as the distance between the point  $P_3$  and the point  $P_4$  and finally  $d_3$  as the distance between the point  $P_5$  and the point  $P_6$ . Each of these distances is calculated using the following formulas:

$$d_1 \mathbf{i} = \mathbf{P}_2 - \mathbf{P}_1, d_2 \mathbf{j} = \mathbf{P}_4 - \mathbf{P}_3 \text{ and } d_3 \mathbf{k} = \mathbf{P}_6 - \mathbf{P}_5.$$
 (11)

Substituting (10) into (11) gives:

$$d_1 \mathbf{i} = \mathbf{A}_2 + \zeta_2 \mathbf{v} - \mathbf{A}_1 - \zeta_1 \mathbf{u},$$

$$d_2 \mathbf{j} = \mathbf{A}_3 + \zeta_4 \mathbf{w} - \mathbf{A}_2 - \zeta_3 \mathbf{v} \text{ and}$$

$$d_3 \mathbf{k} = \mathbf{A}_1 + \zeta_6 \mathbf{u} - \mathbf{A}_3 - \zeta_5 \mathbf{w}.$$
(12)

Using algebraic methods, it is possible to determine  $d_1$ ,  $d_2$ ,  $d_3$  and  $\zeta_i$  as a function of  $\theta$ ,  $\phi$  and  $\sigma$ . A condition, where there is no intersection between bars, is established and includes two aspects: the distance between the bars must be greater than the diameter of the bar  $D_b$ , and the scalar parameters  $\zeta_1$ ,  $\zeta_2$ ,  $\zeta_3$ ,  $\zeta_4$ ,  $\zeta_5$  and  $\zeta_6$  should be in the range of the length of the bar, i.e:

$$d_1, d_2, d_3 \ge D_b$$
 and  $0 \le \zeta_1, \zeta_2, \zeta_3, \zeta_4, \zeta_5, \zeta_6 \le L.$  (13)

The results of the analyses are shown in Fig. 10, 11 and 12. The grey area represents reachable values of  $\sigma$ ,  $\phi$  and  $\theta$ , and the white area represents unreachable values.

Fig. 10 shows the relation  $\theta$  vs  $\sigma$  for all possible values of  $\phi$ . In this figure, if we fix  $\theta=0$ , we can observe two zones for  $\sigma$ . Zone 1 ( $\sigma\in[-\pi/3,2\pi/3]$  rad) corresponds to the clockwise movement of the mechanism, from the value of  $\sigma$  where the bars cross  $(-\pi/3)$  rad) to the value of  $\sigma$  where the bars become parallel  $(2\pi/3)$  rad). On the other hand, zone 2 ( $\sigma\in[2\pi/3,5\pi/3]$  rad) is associated with the counterclockwise movement of the mechanism, from the value of  $\sigma$ , where the bars are parallel  $(2\pi/3)$  rad), to the value of  $\sigma$ , where the bars cross again  $(5\pi/3)$  rad).

Fig. 11 shows a cross section on the  $\sigma$  and  $\theta$  axes for two values of  $\phi$  ( $\phi$  = 0 and  $\phi$  =  $\pi/2$  rad). The two graphs in this figure show the movement of the mechanism in the two vertical and orthogonal planes of 3-D space. In both planes there are two distinct zones as explained for Fig. 10. In the vertical plane of zone 1 (Fig. 11a) the range of  $\theta$  is observed to extend from  $-\pi$  to  $\pi/2$  rad when  $\sigma = \pi/3$  rad. Moving to zone 2, we see that for  $\sigma = \pi$  the allowable range for  $\theta$  is from  $-\pi/2$  to  $\pi$  rad. Shifting the focus to the orthogonal plane (Fig. 11b), zone 1 shows that for  $\sigma$  = 0 the allowable range for  $\theta$  is from  $-\pi$  to  $\pi/2$  rad. Similarly, in zone 2, when  $\sigma$  =  $4\pi/3$ , the range for  $\theta$  shows a similar pattern.

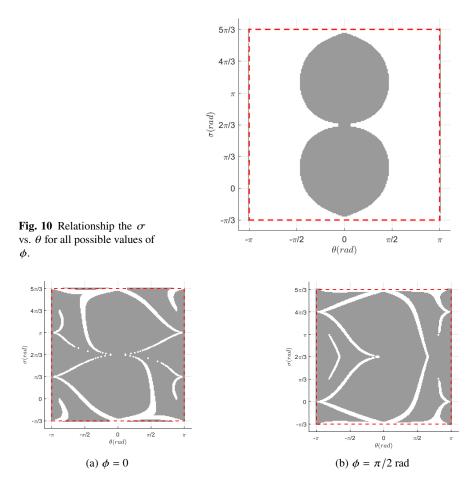


Fig. 11: Cross-section in the  $\sigma$  vs  $\theta$  plane for different  $\phi$  values.

The cross section of  $\phi$  vs.  $\theta$  for different values of  $\sigma$  in zone 1 is shown in Fig. 12. As the value of  $\sigma$  increases, the range of  $\theta$  gradually increases, but then decreases until it reaches a minimum value. However, it is important to note that the maximum range of  $\theta$  in zone 1 is within the interval  $[-\pi/2, \pi/2]$  rad.

After analysing the kinematic workspace, the following chapters will focus exclusively on zone 1. Therefore, the operating limits are defined as follows  $\theta \in [-\pi/2, \pi/2]$  rad,  $\phi \in [-\pi, \pi]$  rad and  $\sigma \in [-\pi/3, 2\pi/3]$  rad.

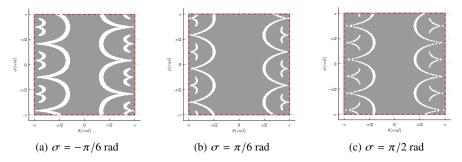


Fig. 12: Cross-section in the  $\phi$  vs  $\theta$  plane for different  $\sigma$  values.

## 3.4 Stability Conditions

According to Burkhardt [10], the choice of lengths for the three final tendons, each corresponding to one side, plays a crucial role in ensuring the stability of the prism mechanism proposed in his research. Burkhardt mentioned that as the prism ends twist, some points come closer together and then move apart. The binding of the side tendons at the closest point is crucial for stability. The structure can only change by increasing the distance between these points, which is prevented by the short tendons, and this basic concept underlies all tensegrity designs that have been explored. It is therefore important to determine the minimum length of the cables for the mechanism proposed keeping its internal DOF fixed ( $\phi = \theta = 0$ ) and only rotates around the vertical axis for torsional effects.

The length of the cables and bars can be defined using the parameters shown in Fig. 3 and Table 1. Since the cable length equation has been defined in subsection 3.2, the specific cable length equation in this case, together with the kinematic constraint for the bar length, is defined as follows:

$$\ell^2 = z^2 + \frac{2b^2}{3} - \frac{2b^2 \cos(2\psi - \sigma)}{3} \quad \text{and}$$
 (14)

$$L^{2} = z^{2} + \frac{2b^{2}}{3} + \frac{b^{2}\cos(\sigma)}{3} - \frac{\sqrt{3}b^{2}\sin(\sigma)}{3}.$$
 (15)

Finding  $z^2$  in (15):

$$z^{2} = L^{2} - \frac{2b^{2}}{3} - \frac{b^{2}\cos(\sigma)}{3} + \frac{\sqrt{3}b^{2}\sin(\sigma)}{3}.$$
 (16)

and replacing (16) in (14) gives:

$$\ell^2 = L^2 - \frac{b^2 \cos(\sigma)}{3} + \frac{\sqrt{3}b^2 \sin(\sigma)}{3} - \frac{2b^2 \cos(2\psi - \sigma)}{3}.$$
 (17)

For (17), finding the minimum value of the cable length for the twist:

$$\min_{\sigma} \left[ f(\sigma) = L^2 - \frac{b^2 \cos(\sigma)}{3} + \frac{\sqrt{3}b^2 \sin(\sigma)}{3} - \frac{2b^2 \cos(2\psi - \sigma)}{3} \right], \tag{18}$$

where

$$\frac{df}{d\sigma} = -\frac{b^2}{3} \left( 2\sin(2\psi - \sigma) - 2\sin(\sigma + \frac{\pi}{3}) \right) = 0,\tag{19}$$

implies

$$\sin(2\psi - \sigma) = \sin(\sigma + \frac{\pi}{3}). \tag{20}$$

Finally,

$$2\psi - \sigma = \sigma + \frac{\pi}{3} \quad \Rightarrow \quad \sigma = \psi - \frac{\pi}{6}.$$
 (21)

Changing  $\psi$  induces a corresponding adjustment in  $\sigma$  with the same direction and magnitude, maintaining a consistent offset of  $\pi/6$  rad. This adjustment is essential for the stability of the system. Given that  $\psi = \pi/12$  rad in the proposed mechanism, the optimal configuration for maintaining stability is achieved when  $\sigma = -\pi/12$  rad. The feasibility of achieving this configuration using actuators will be examined in the following section.

## 4 Static Equilibrium Conditions

This chapter examines the geometry of the proposed spatial mechanism to ensure stability, particularly in the context of static equilibrium conditions. The subsection 4.1 provides an analysis of the behaviour of the system keeping its internal DOF fixed ( $\phi = \theta = 0$ ) and assesses the feasibility of managing the cable forces to maintain stability. On the other hand, subsection 4.2 presents an alternative solution, as the original geometry alone may not ensure stability under these conditions. This alternative involves introducing the force of a fourth cable positioned at the centre of the two platforms of the mechanism.

#### 4.1 System at Rest

Considering that the mechanism will be integrated into a robot manipulator, we are investigating the influence of rigid angular motions  $(\alpha, \beta)$  on the structural integrity of the proposed mechanism, while keeping its internal DOF fixed  $(\phi = \theta = 0)$ . Exploring the system under these conditions provides valuable insights into its equilibrium and cable forces, and offers a comprehensive review of its feasibility when considering the involvement of actuators and their force limitations.

The equilibrium is analysed using the Newton-Euler equations:

$$\sum \mathbf{F} = 0 \quad \text{and} \quad \sum \mathbf{M} = 0. \tag{22}$$

Considering the forces in the bars ( $\mathbf{F}_{b1}$ ,  $\mathbf{F}_{b2}$ ,  $\mathbf{F}_{b3}$ ) and in the cables ( $\mathbf{F}_{c1}$ ,  $\mathbf{F}_{c2}$ ,  $\mathbf{F}_{c3}$ ), together with the gravitational force ( $\mathbf{F}_{g}$ ), the sum of the forces in equilibrium is expressed:

$$\mathbf{F}_{b1} + \mathbf{F}_{b2} + \mathbf{F}_{b3} + \mathbf{F}_{c1} + \mathbf{F}_{c2} + \mathbf{F}_{c3} + \mathbf{F}_{g} = 0,$$
 (23)

and the sum of the moments at the point  $o_3$  is expressed:

$$\mathbf{A}_{6}\mathbf{o}_{3} \times \mathbf{F}_{b1} + \mathbf{A}_{4}\mathbf{o}_{3} \times \mathbf{F}_{b2} + \mathbf{A}_{5}\mathbf{o}_{3} \times \mathbf{F}_{b3} + \mathbf{B}_{4}\mathbf{o}_{3} \times \mathbf{F}_{c1} + \mathbf{B}_{5}\mathbf{o}_{3} \times \mathbf{F}_{c2} + \mathbf{B}_{6}\mathbf{o}_{3} \times \mathbf{F}_{c3} = 0.$$
(24)

The forces acting in the bars can be defined as follows:

$$\mathbf{F}_{b1} = f_{b1} \frac{\mathbf{A}_6 - \mathbf{A}_1}{L}, \, \mathbf{F}_{b2} = f_{b2} \frac{\mathbf{A}_4 - \mathbf{A}_2}{L} \text{ and } \mathbf{F}_{b3} = f_{b3} \frac{\mathbf{A}_5 - \mathbf{A}_3}{L},$$
 (25)

where  $f_{b1} < 0$ ,  $f_{b2} < 0$ , and  $f_{b3} < 0$ , this phenomenon can be attributed to a technological aspect, specifically the magnetic nature of the spherical joints, which can lead to disassembly if subjected to excessive tensile forces.

The forces acting in the cables can be defined as follows:

$$\mathbf{F}_{c1} = f_{c1} \frac{\mathbf{B}_4 - \mathbf{B}_1}{l_1}, \, \mathbf{F}_{c2} = f_{c2} \frac{\mathbf{B}_5 - \mathbf{B}_2}{l_2} \text{ and } \mathbf{F}_{c3} = f_{c3} \frac{\mathbf{B}_6 - \mathbf{B}_3}{l_3},$$
 (26)

where  $f_{c1} > 0$ ,  $f_{c2} > 0$ ,  $f_{c3} > 0$  to achieve the tensegrity property.

The gravitational force is defined as:

$$\mathbf{F}_g = m \ \mathbf{g}. \tag{27}$$

Solving (25), (26), (27) in (23) and (24) will yield the expressions for  $f_{c1}$ ,  $f_{c2}$ , and  $f_{c3}$ ,  $f_{b1}$ ,  $f_{b2}$ , and  $f_{b3}$  which are of interest for studying stability and feasibility of the proposal mechanism. Therefore, factoring these equations, in order to find the mathematical expression for the cable tensions, allows us to derive the following expression:

$$\begin{bmatrix} \mathbf{A}_c & \mathbf{A}_b \\ \mathbf{B}_c & \mathbf{B}_b \end{bmatrix} \begin{pmatrix} f_c \\ f_b \end{pmatrix} = \begin{pmatrix} -m \ \mathbf{g} \\ 0 \end{pmatrix}$$
 (28)

where 
$$f_c = (f_{c1}, f_{c2}, f_{c3})^T$$
 and  $f_b = (f_{b1}, f_{b2}, f_{b3})^T$ .

Considering the equation provided in (28), the cable tensions can be defined as follows:

$$f_c = -(\mathbf{A}_c - \mathbf{A}_b \; \mathbf{B}_b^{-1} \; \mathbf{B}_c)^{-1} m \; \mathbf{g} \; . \tag{29}$$

Due to the complexity of this expressions, the detailed equations will not be included in this document. However, the underlying variables on which these ex-

pressions depend are listed below:

$$f_{c1} = h(\sigma, \alpha, \beta, \psi, b, L, m, g), \quad f_{c1} > 0,$$
  
 $f_{c2} = h(\sigma, \alpha, \beta, \psi, b, L, m, g), \quad f_{c2} > 0 \quad \text{and}$   
 $f_{c3} = h(\sigma, \alpha, \beta, \psi, b, L, m, g), \quad f_{c3} > 0.$  (30)

In subsection 3.4, it was deduced that for  $\psi = \pi/12 \,\mathrm{rad}$ , the system would be stable when  $\sigma = -\pi/12 \,\mathrm{rad}$ . Therefore, the subsequent analysis will examine the relationship between cable tensions  $f_{c1}$ ,  $f_{c2}$ ,  $f_{c3}$  and  $\sigma$ , aiming to confirm the condition for stability. For this analysis, the simplest context will be considered, where  $\alpha = 0$  and  $\beta = 0$ . This context allows for the simplification of equations for  $f_{c1}$ ,  $f_{c2}$ , and  $f_{c3}$ , satisfying the following conditions:  $l = l_1 = l_2 = l_3$  and  $f_c = f_{c1} = f_{c2} = f_{c3}$  and  $f_b = f_{b1} = f_{b2} = f_{b3}$ .

In this scenario, the complex set of equations provided in (23) and (24) are simplified to the concise form of the sum of forces and moments represented respectively by:

$$\frac{3 f_b z}{L} + \frac{3 f_c z}{l} - m g = 0 \quad \text{and}$$
 (31)

$$f_b l \left( \sin(\sigma) + \sqrt{3} \cos(\sigma) \right) + 2 f_c L \sin(2\psi - \sigma) = 0.$$
 (32)

Solving the above equations gives the resulting expressions for  $f_b$  and  $f_c$ :

$$f_b = \frac{m g L \sin(2\psi - \sigma)}{3 z \left(\sin(2\psi - \sigma) - \sin(\sigma + \pi/3)\right)} \quad \text{and}$$
 (33)

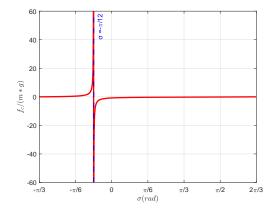
$$f_c = \frac{m g l \sin(\sigma + \pi/3)}{3 z \left(\sin(2\psi - \sigma) - \sin(\sigma + \pi/3)\right)}.$$
 (34)

In these equations, the variables z and l can be defined according to the expressions provided in (16) and (17). It is important to note that the cable tension  $f_c$  must be positive to satisfy the tensegrity condition.

Fig. 13 illustrates  $f_c$  for  $\sigma \in [-\pi/3, 2\pi/3]$  rad. In this figure is shown that  $f_c$  adhere to the tensegrity condition only for torsion values greater than  $-\pi/3$  rad and less than  $-\pi/12$  rad. Hence, a new range for torsion is defined.

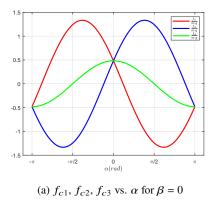
Also in this figure,  $f_c$  exhibits an infinite increase when  $\sigma = -\pi/12$  rad. This behavior indicates that the system reaches a singularity where the length of the cables becomes minimal, as illustrated in Eq.(18) and Eq.(19). These equations constitute a portion of the Jacobian matrix of the system. and when their value becomes zero, it leads to the system entering a singularity, rendering it uncontrollable.

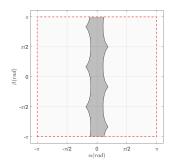
Therefore, we will analyse the behaviour of the system by choosing another torsion value within the new range where the cable forces are positive ( $\sigma \in [-\pi/3, -\pi/12]$  rad) and also rotating it in 3-D space  $(\alpha, \beta)$ . This involves using (30) to create expressions for  $f_{c1}$ ,  $f_{c2}$  and  $f_{c3}$ . When searching for an alternative



**Fig. 13**  $f_c$  vs.  $\sigma$  for system keeping its internal DOF fixed  $(\phi = \theta = 0)$  and considering  $\alpha = 0$  and  $\beta = 0$ ).  $f_c$  becomes infinite when  $\sigma = -\pi/12$  rad.

torsion value, it is essential to ensure that for this particular torsion the system retains the ability to rotate over the whole range of  $\alpha \in [-\pi, \pi]$  rad and  $\beta \in [-\pi, \pi]$  rad, while at the same time satisfying the condition that the  $f_{c1}$ ,  $f_{c2}$  and  $f_{c3}$  remain strictly greater than zero. Using the equations provided in (30) and choosing a torsion value ( $\sigma = -\pi/6$  rad), the analysis of  $f_{c1}$ ,  $f_{c2}$  and  $f_{c3}$  is performed and the results are shown in Fig. 14. Fig. 14a illustrates that at some point during the orientation around  $\alpha$  considering  $\beta = 0$ , the cable tensions become negative, violating the specified condition of tensegrity. Furthermore, in Fig. 14b, a detailed analysis of the  $\beta$  versus  $\alpha$  region reveals a distinct pattern. In this plot, positive cable tensions are highlighted in grey, while negative cable tensions are highlighted in white. It is clear that there are specific combinations of  $\alpha$  and  $\beta$  where the cable forces deviate from being strictly positive.





(b) Feasible orientation range for  $\alpha$  and  $\beta$  with  $\{f_{c1}, f_{c2}, f_{c3}\} > 0$ 

Fig. 14: System keeping its internal DOF fixed ( $\phi = \theta = 0$ ) under angular rigid orientation around  $\alpha$  and  $\beta$  and a torsion of  $\sigma = -\pi/6$  rad.

In light of this consideration, the analysis is directed towards examining the correlation between the angular rigid orientation range around  $(\alpha, \beta)$  and the torsion value  $\sigma$ . The results, illustrated in Fig. 15a, show that as the torsion value  $\sigma$  decreases, the orientation range around  $\alpha$  decreases proportionally. The overall goal is to achieve an orientation range of  $\alpha$  equal to  $\pi$ ; however, it becomes apparent that this goal is unattainable. Fig.15b and Fig.15c give an insight into the feasible values of  $\alpha$  and  $\beta$  for the points A and C shown in Fig. 15a, while point B was previously shown in Fig. 14b. Unfortunately, none of these cases allows a complete orientation.

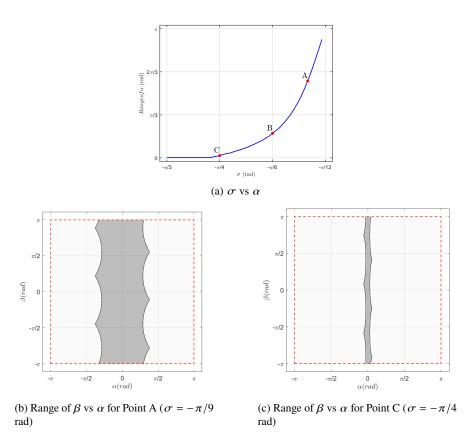


Fig. 15: System keeping its internal DOF fixed ( $\phi = \theta = 0$ ) under angular rigid orientation around  $\alpha$  and  $\beta$  with different values of torsion.

To mitigate this problem and prevent cable slack, two possible design solutions are presented, as shown in Fig. 16. The first solution involves the introduction of a new central cable of length  $l_4$ , connected to  $o_0$  and  $o_3$ , which maintains the torsional angle of the mobile platform by applying a new tension to it. The second solution is to insert a leg between these two points. This leg is a driving form consisting of two

universal joints at its ends and a prismatic joint in the middle. The angular offset between the connection points at the two tips makes it possible to fix the torsion angle of the mechanism.

Each solution has its own advantages and disadvantages. The first solution offers increased system flexibility by allowing torsional variation through the force applied to this cable. However, the disadvantage is that the control of the force variation in this fourth cable is very sensitive. On the other hand, the second solution offers the advantage of increased system stiffness. However, it reduces the number of DOF by sacrificing torsion, which remains fixed in its spatial rotation. In addition, this adjustment introduces more inertia (due to the new mass) and increases the likelihood of collisions between the bars.

The following subchapter analyses the behaviour of the system keeping its internal DOF fixed ( $\phi = \theta = 0$ ) and taking into account the presence of a fourth cable; the study of the second option will be part of future studies.

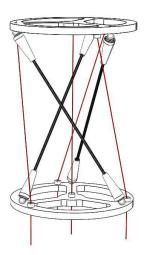




Fig. 16: Two potential design solutions for achieving a full orientation in  $\alpha$  and  $\beta$  accomplishing the condition of tensegrity ( $\{f_{c1}, f_{c2}, f_{c3}\} > 0$ ).

#### 4.2 System at rest adding a fourth cable

For static analysis, the force in the fourth cable is added:

$$\mathbf{F}_{c4} = f_{c4} \, \frac{\mathbf{o}_3 - \mathbf{o}_0}{l_4},\tag{35}$$

and the sum of forces is presented:

$$\mathbf{F}_{b1} + \mathbf{F}_{b2} + \mathbf{F}_{b3} + \mathbf{F}_{c1} + \mathbf{F}_{c2} + \mathbf{F}_{c3} + \mathbf{F}_{c4} + \mathbf{F}_{g} = 0.$$
 (36)

The sum of the moments remains consistent with the expression in (24). By including the force  $\mathbf{F}_{c4}$  in the sum of forces, a solvable system of equations is obtained. This leads to updated expressions for  $f_{c1}$ ,  $f_{c2}$  and  $f_{c3}$ . Therefore, factoring these equations to find the mathematical expression for the cable tensions allows us to derive the following expression:

$$\begin{bmatrix} \mathbf{A}_c & \mathbf{A}_{c4} & \mathbf{A}_b \\ \mathbf{B}_c & 0 & \mathbf{B}_b \end{bmatrix} \begin{pmatrix} f_c \\ f_{c4} \\ f_b \end{pmatrix} = \begin{pmatrix} -m & \mathbf{g} \\ 0 \end{pmatrix}$$
 (37)

where  $f_c = (f_{c1}, f_{c2}, f_{c3})^T$  and  $f_b = (f_{b1}, f_{b2}, f_{b3})^T$ . By moving the terms associated with  $\mathbf{F}_{c4}$  from the equation (37) on the opposite side of the equality:

$$\begin{bmatrix} \mathbf{A}_c & \mathbf{A}_b \\ \mathbf{B}_c & \mathbf{B}_b \end{bmatrix} \begin{pmatrix} f_c \\ f_b \end{pmatrix} = \begin{pmatrix} -m \ \mathbf{g} - \mathbf{A}_{c4} \ f_{c4} \\ 0 \end{pmatrix}. \tag{38}$$

where  $f_{c4}$  is defined as the tuning parameter for the tension of the fourth cable of the mechanism. Taking into account the equation given in (38), the cable tensions can be defined as follows:

$$f_c = -(\mathbf{A}_c - \mathbf{A}_b \ \mathbf{B}_b^{-1} \ \mathbf{B}_c)^{-1} (m \ \mathbf{g} + \mathbf{A}_{c4} \ f_{c4}). \tag{39}$$

Due to their complexity, the detailed equations are not explicitly presented in this document. However, similar to the previous analysis, the underlying variables that influence these expressions are listed below:

$$f_{c1} = h(\sigma, \alpha, \beta, \psi, b, L, m, g, f_{c4}), \quad f_{c1} > 0,$$
  

$$f_{c2} = h(\sigma, \alpha, \beta, \psi, b, L, m, g, f_{c4}), \quad f_{c2} > 0 \quad \text{and}$$

$$f_{c3} = h(\sigma, \alpha, \beta, \psi, b, L, m, g, f_{c4}), \quad f_{c3} > 0.$$
(40)

Continuing with the example presented in the previous chapter, the design with  $\sigma = -\pi/6$  rad for the torsion of the system is selected and a tension  $f_{c4}$  is applied. Fig. 14b, presented in the previous subchapter, shows the  $\beta$  vs.  $\alpha$  range, revealing instances where the cable tensions were not positive when the fourth cable was not present. On the other hand, Fig. 17 illustrates the behaviour of the  $\beta$  vs.  $\alpha$  region when the fourth cable is present and for different tension values. It can be seen that as the tension  $f_{c4}$  increases, the area of the  $\beta$  vs.  $\alpha$  region also increases, ensuring that  $f_{c1}$ ,  $f_{c2}$  and  $f_{c3}$  are positive. Therefore, with the appropriate tension  $f_{c4}$ , the tensegrity property can be satisfied.

As observed in Figs. 15 and 17, the range of orientation in  $\alpha$  and  $\beta$  varies as we change  $\sigma$  and  $f_{c4}$  respectively. It is therefore crucial to examine the relationship between the range of  $\alpha$  and  $\beta$  and the tension of the fourth cable  $(f_{c4})$  and the torsion

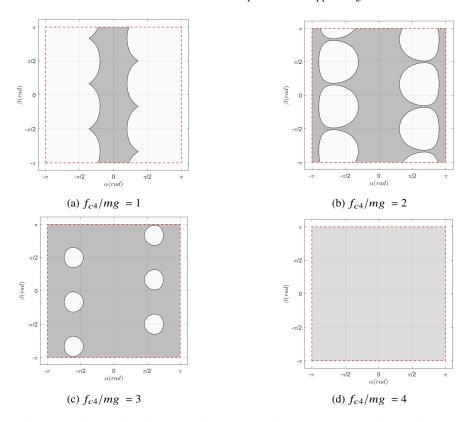
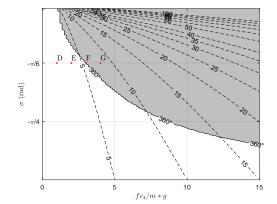


Fig. 17: Feasible orientation range for  $\alpha$  and  $\beta$  with the system keeping its internal DOF fixed ( $\phi = \theta = 0$ ) and torsion  $\sigma = -\pi/6$  rad.

( $\sigma$ ). The importance of this analysis is to identify the values of  $f_{c4}$  and  $\sigma$  that allow a complete orientation around  $\alpha$  and  $\beta$  while satisfying the tensegrity conditions ( $\{f_{c1}, f_{c2}, f_{c3}\} > 0$ ).

Fig. 18 shows the result of this analysis and illustrates the limiting relationship between  $f_{c4}$  and  $\sigma$ , ensuring a full range of  $\alpha$  and  $\beta$  without compromising the tensegrity condition (grey area). As can be seen, an increase in the tension allows a greater range of torsional rotation where the tensegrity condition is satisfied. The figure also shows points D, E, F, G, which represent the values when  $f_{c4}$  is equal to 1, 2, 3, 4 times mg respectively, in the case where the torsion considers a value of  $\sigma$  equal to  $-\pi/6$  rad. It can be seen that points D and E are clearly outside the grey zone (area where a full range of orientation for  $\alpha$  and  $\beta$  is ensured without compromising tensegrity). In the case of point F, it is very close to the boundary but still outside the zone, and only point G falls within the grey zone. This observation is consistent with the results shown in Fig. 17.

Also, by analysing the behaviour of  $(f_{c1} + f_{c2} + f_{c3} + f_{c4})/(mg)$ , for this minimal relationship  $f_{c4}/(mg)$  vs.  $\sigma$ , we want to determine the optimal value of  $\sigma$  where the sum of tensions is minimised, as also shown in Fig. 18.



**Fig. 18** Relationship between  $f_{c4}$  and  $\sigma$  ensuring the tensegrity condition for the system keeping its internal DOF fixed  $(\phi = \theta = 0)$  considering the sum  $(f_{c1} + f_{c2} + f_{c3} + f_{c4}) / (mg)$ .

The optimal value of  $\sigma$ , which corresponds to the minimum of the nominal sum of forces  $(f_{c1} + f_{c2} + f_{c3} + f_{c4})/(mg) = 1.93$ ), while satisfying the tensegrity conditions for any orientation in  $\alpha$  and  $\beta$ , and is found to be  $\sigma = -19.1^{\circ}$ .

It can therefore be concluded that the tensegrity condition can be solved by adding a fourth cable between  $o_0$  and  $o_3$ . Once this fourth cable is added, it is important to fix its tension to ensure that  $f_{c1}$ ,  $f_{c2}$  and  $f_{c3}$  are positive.

## 5 Conclusions and future work

This paper introduces a spatial mechanism comprising two platforms, fixed and mobile, interconnected by cables and bars. Its key advantage lies in its simplicity and lightweight design, distinguishing it from previous research. This characteristic makes the mechanism suitable for constructing collaborative robots (cobots) intended for human-machine interaction without causing harm. The mechanical integration constraint imposes a non-coincident arrangement of cable and bar endpoints, introducing an angle between them. This feature adds an interesting aspect for stability analysis.

The analysis reveals that the system encounters a singularity at a torsion value intended for achieving stability. To address this, the introduction of a fourth cable is proposed. Precise tuning of the tension in this additional cable becomes crucial to fix the torsion value, ensuring that all cables remain under tension, satisfying the tensegrity condition.

Future work aims to delve into the system's behavior as the torsion value  $(\sigma)$  approaches the singularity at  $\sigma = -\pi/12$  rad. Additionally, exploring the integration

of springs in cables  $l_1$ ,  $l_2$ , and  $l_3$  is suggested to enhance system stability, particularly during complete rotation against gravity. However, the potential drawbacks of this modification require thorough analysis. Finally, research is expected to investigate the substitution of the fourth cable with a leg as a potential design modification.

#### References

- 1. A. C. Pereira and F. Romero. A review of the meanings and the implications of the industry 4.0 concept. *Procedia Manufacturing*, 13:1206–1214, 2017.
- A. Weiss, A. K. Wortmeier, and B. Kubicek. Cobots in industry 4.0: A roadmap for future practice studies on human–robot collaboration. *IEEE Transactions on Human-Machine Systems*, 51(4):335–345, 2021.
- E. Colgate, A. Bicchi, M. A. Peshkin, and J. E. Colgate. Safety for physical human-robot interaction. In Springer handbook of robotics, pages 1335–1348. 2008.
- G. Michalos, S. Makris, P. Tsarouchi, T. Guasch, D. Kontovrakis, and G. Chryssolouris. Design considerations for safe human-robot collaborative workplaces. *Procedia CIrP*, 37:248–253, 2015.
- 5. D.G. Emmerich. Construction of self-powered networks, 1964. French Patent No. 1,377,290.
- K. D. Snelson. Tensegrity structures, 1965. U.S. Patent No. 3,169,611. Washington, DC: U.S. Patent and Trademark Office.
- I. A. Bonev, D. Zlatanov, and C. M. Gosselin. Advantages of the modified euler angles in the design and control of pkms. pages 171–188, April 2002.
- 8. R. E. Skelton and M. C. De Oliveira. Tensegrity systems, volume 1. Springer, 2009.
- Y. Liu, Q. Bi, X. Yue, J. Wu, B. Yang, and Y. Li. A review on tensegrity structures-based robots. *Mechanism and Machine Theory*, 168:104571, 2022.
- 10. R. W. Burkhardt. A practical guide to tensegrity design. Cambridge USA, 2008.
- M. Arsenault and C. M. Gosselin. Kinematic and static analysis of a three-degree-of-freedom spatial modular tensegrity mechanism. *The International Journal of Robotics Research*, 27(8):951–966, 2008.
- M. Q. Marshall. Analysis of tensegrity-based parallel platform devices. 2003. Doctoral dissertation, University of Florida.
- Matthieu Furet and Philippe Wenger. Kinetostatic analysis and actuation strategy of a planar tensegrity 2-x manipulator. ASME J. of Mechanisms and Robotics, 11(6):060904, 2019.
- 14. Benjamin Fasquelle, Parag Khanna, Christine Chevallereau, Damien Chablat, Denis Creusot, Stephane Jolivet, Philippe Lemoine, and Philippe Wenger. Identification and control of a 3-x cable-driven manipulator inspired from the bird neck. *Journal of Mechanisms and Robotics*, pages 1–25, 2021.
- J. M. Mirats-Tur and J. Camps. A three-dof actuated robot. *IEEE robotics & automation magazine*, 18(3):96–103, 2011.
- B. Fasquelle, M. Furet, P. Khanna, D. Chablat, C. Chevallereau, and P. Wenger. A bioinspired 3-dof light-weight manipulator with tensegrity x-joints. In 2020 IEEE International Conference on Robotics and Automation (ICRA), pages 5054–5060. IEEE, May 2020.
- Yong-Jae Kim, Jong-In Kim, and Wooseok Jang. Quaternion joint: Dexterous 3-dof joint representing quaternion motion for high-speed safe interaction. In 2018 IEEE/RSJ International Conference on Intelligent Robots and Systems (IROS), pages 935–942. IEEE, 2018.
- 18. I. John, S. Mohan, and P. Wenger. Kinetostatic analysis of a spatial cable-actuated variable stiffness joint. *Journal of Mechanisms and Robotics*, pages 1–21, 2023.
- 19. M. Sheikhpour and M. Bamdad. Forward kinematic analysis of tensegrity mechanism using hybrid method. In 2017 5th RSI International Conference on Robotics and Mechatronics (ICRoM), pages 564–569, October 2017.
- M. Stock and K. Miller. Optimal kinematic design of spatial parallel manipulators: application to linear delta robot. J. Mech. Des., 125(2):292–301, 2003.